OPEN ACCESS

Simulation Study of Enhancement Mode Multi-Gate Vertical Gallium Oxide MOSFETs

To cite this article: Junsung Park and Sung-Min Hong 2019 *ECS J. Solid State Sci. Technol.* **8** Q3116

JSS Focus Issue on Gallium Oxide Based Materials and Devices

Simulation Study of Enhancement Mode Multi-Gate Vertical Gallium Oxide MOSFETs

Junsung Park and Sung-Min Hong [z]

School of Electrical Engineering and Computer Science, Gwangju Institute of Science and Technology, Buk-gu, Gwangju 61005, Korea

In this study, the state-of-the-art vertical gallium oxide MOSFET with the fin shaped source is numerically investigated. With the simulation environment, whose results for the electrical characteristics are in close agreement with the available experimental results, the impact of the fin shape is studied. It is found that a rectangular fin with a height of 1.0 μm and a width of 0.3 μm can give a low on-resistance per unit area and a low drain-induced barrier lowering (DIBL) simultaneously. Moreover, the tapered fins are simulated to estimate the sensitivity of the on-resistance, the DIBL, and the subthreshold slope.

 [DOI: 10.1149/2.0181907jss]

Manuscript received February 11, 2019. Published March 8, 2019. *This paper is part of the JSS Focus Issue on Gallium Oxide Based Materials and Devices.*

The beta gallium oxide ($\beta - Ga_2O_3$) is a wide bandgap semiconductor material, which is an ideal candidate for the power device application.[1–4] Various superior material properties such as wide bandgap (E_g= 4.85 eV), high breakdown field (approximately 8 MV/cm[5,6]), and high Baliga's figures of merit are reported.[3,4] In addition to the advantages due to the superior material properties, it is possible to manufacture a cost-effective wafer with a large diameter by using the bulk growth method. The Czochralski(CZ),[7,8] floating zone (FZ),[7] and edge-defined film-fed growth (EFG)[9,10] methods are reported. The availability of the native substrate is quite an important advantage of $\beta - Ga_2O_3$ over other wide bandgap materials.

Even through the $\beta - Ga_2O_3$ based device technology is at an early stage of the technology development, many reports have already been made to show its potential for future power devices. The performance of some recent research results is comparable to that of the state-of-the-art SiC or GaN-based power devices.[11–13] The rectifier based on the diode structure has been reported.[13–17] Moreover, power MOSFETs with high-efficiency and high-voltage operation have been under development. The planar MOSFET,[18] the field-plate(FP) MOSFET,[19–23] and the multi-gate MOSFET[11,12,24,25] have been investigated.

Recently, various vertical MOSFETs are also reported. Because of its structural benefit, the vertical MOSFET structure has been extensively applied to the power MOSFET application.[26–31] In particular, the vertical MOSFET structures with the vertical fin shaped source have plausible characteristics of the enhancement mode operation, the high on current (I_{on}), and the high breakdown voltage.[29,30] The typical structure of the vertical MOSFET with the fin shaped source is illustrated in Fig. 1.

The technology development can be much accelerated by using the technology computer-aided design (TCAD) simulation appropriately. In addition to the progress in the device fabrication, there have been a few reports about the TCAD simulation of the $\beta - Ga_2O_3$ devices.[32–36] For the Schottky barrier diodes, some studies are performed on the impact of the field plate.[33–35] However, the systematic investigation of the device performance based on the TCAD simulation is rarely found.

In this work, the TCAD simulation is employed to investigate the electrical performance of the multi-gate vertical $\beta - Ga_2O_3$ MOSFETs. The simulation setup for the $\beta - Ga_2O_3$ based devices is suggested. The physical soundness of our simulation setup is verified by comparing our results with the experimental results available from the literature.[29,30] The impact of the device structure on the electrical performance is investigated.

The structure of this work is as follows. In Simulation Setup section, the simulation setup adopted in this work is briefly explained. The simulation results for the enhancement mode multi-gate vertical $\beta - Ga_2O_3$ MOSFETs are presented in Simulation Results and Discussion section. After comparing our simulation results with the experimental results in the literature, the design optimization for the fin shape is performed. The conclusion is made in Conclusion section.

Simulation Setup

In this section, the simulation setup for the $\beta - Ga_2O_3$ based devices is introduced. Since $\beta - Ga_2O_3$ has gained great interest from the device engineering society quite recently, the material models such as the mobility model and the impact ionization model should be carefully examined. After reviewing some models suggested by recent research works, the selected model parameters are explicitly shown.

Mobility model.—In the TCAD simulation, the carrier mobility is calculated by combining several effects. Usually, three components – the dependencies on the doping concentration, the high-field saturation effect, and the surface effect – are considered. Since the electrons are

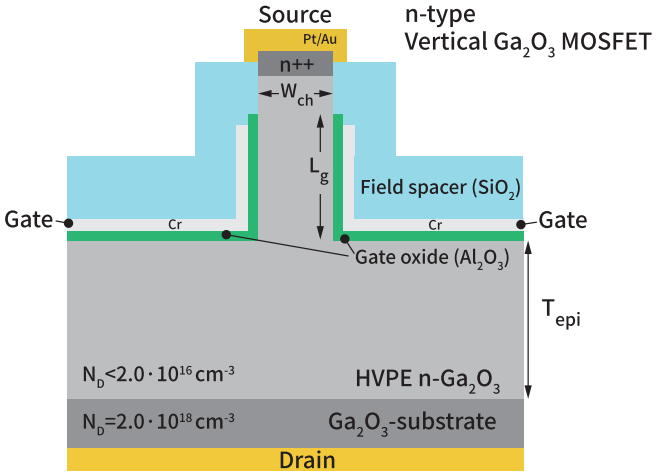

Figure 1. Schematic cross sections of the $\beta - Ga_2O_3$ vertical MOSFET.

[z]E-mail: smhong@gist.ac.kr

Table I. Arora Model : Optimized model parameters for $\beta - Ga_2O_3$.

Parameter	Electrons	Holes	Unit
A_{min}	13	0.016	$cm^2/V \cdot s$
α_m	−0.57	−0.57	1
A_d	235	0.2	$cm^2/V \cdot s$
α_d	0.78	0.78	1
A_N	$1.10 \cdot 10^{18}$	$1.25 \cdot 10^{17}$	cm^{-3}
α_N	2.4	2.4	1
A_a	0.78	0.78	1
α_a	−0.146	−0.146	1

located at the fin center in the vertical MOSFET, it is expected that the surface effects do not play a significant role. Therefore, the doping and high-field dependencies are included in this work.

Theoretical approaches for the mobility calculation can be found in the literature.[37–41] The experimental results of the doping-dependent mobility is summarized and an analytic expression has been suggested.[38] In order to adopt those results in the commercial TCAD simulator, the model parameters of the Arora model,[42] which is the standard mobility model for the doping dependence, are adjusted. According to the Arora model, the doping dependent mobility is given as

$$\mu_{doping} = \mu_{min} + \frac{A_d}{1 + \left(\frac{N_{A,0}+N_{D,0}}{N_O}\right)^{A*}}, \quad [1]$$

$$\mu_{min} = A_{min} \cdot \left(\frac{T}{300K}\right)^{\alpha_m}, \qquad \mu_d = A_d \cdot \left(\frac{T}{300K}\right)^{\alpha_d} \quad [2]$$

$$N_0 = A_N \cdot \left(\frac{T}{300K}\right)^{\alpha_N}, \qquad A^* = A_a \cdot \left(\frac{T}{300K}\right)^{\alpha_a}, \quad [3]$$

where A_{min}, A_d, A_N, and A_* are material-dependent model parameters and T is the temperature. The model parameters are adjusted to obtain a reasonable agreement with the model,[38] as shown in Fig. 2a. Table I shows the optimized model parameters for $\beta - Ga_2O_3$.

As much as the high field saturation is concerned, the standard Caughey-Thomas velocity saturation model is adopted.[43] The experimental value of the electron saturation velocity is known to be 2.5×10^7 cm/s.[3,4] This value is applied to our simulation without modification.

Impact ionization model.—Similar to the mobility model, there are some theoretical approaches to calculate the coefficients used in the impact ionization model.[44,45] In addition, a model using the experimental results is also presented.[35] According to the van Overstraeten - de Man model which is based on the Chynoweth model, the impact ionization coefficient α is given by

$$\alpha(E) = \gamma a \exp\left(-\frac{\gamma b}{E}\right), \quad [4]$$

$$\gamma = \frac{\tanh\left(\frac{\hbar\omega_{op}}{2k_B T_0}\right)}{\tanh\left(\frac{\hbar\omega_{op}}{2k_B T}\right)}, \quad [5]$$

where a and b are the material-dependent model parameters. In this work, $a = 7.06 \cdot 10^5$ cm^{-1} and $b = 2.1 \cdot 10^7$ V/cm·s are adopted. These values are taken from the existing model[44] without modification.

Simulation Results and Discussion

Simulation results for vertical MOSFETs.—The $\beta - Ga_2O_3$ vertical MOSFET with the fin shaped source is numerically simulated. In order to verify the simulation model, the simulation is conducted for the MOSFET structure as presented in the Reference 29. Fig. 1 shows the schematic illustration of the overall structure. The n-type bulk $\beta - Ga_2O_3$ (001) substrate with a high doping density is used. The drain contact is formed at the bottom of the substrate. In the TCAD simulation, the substrate thickness is 2 μm. The epitaxial drift channel, whose thickness (T_{epi}) is 9 μm, is doped with n-type dopants. The doping concentration of the drift region is tuned as $1.45 \cdot 10^{16} cm^{-3}$ to fit the experimental electric characteristics. This value is well matched with the epitaxial condition ($< 2.0 \times 10^{16} cm^{-3}$).[38] The vertical fin channel has a thickness (W_{ch}) of 0.44 μm and the gated channel length (L_g) is 0.80 μm. The Al_2O_3 gate dielectric, whose thickness is 30 nm, is isotropically deposited on the vertical fin and the top surface of the drift region. The metal gate contact is wrapped over the gate dielectric. The source underlap region is 100 nm-long and the drain contact is formed at the top of the fin structure. In this work, the TCAD simulation is performed with a commercial semiconductor device simulator.[46]

Fig. 3 shows I_D-V_{GS} characteristics of the vertical $\beta - Ga_2O_3$ MOSFET in the semi-log scale. The gate work function (ϕ_{gate}) is tuned with the experimental results. The subthreshold slope (SS) and the on-current are in close agreement with the experimental results. The SS is measured as 85 mV/dec when the drain current is 1 mA/cm^2. The threshold voltage (V_{th}) is determined as 0.95V. The maximum current density at the gate voltage of 5 V is as high as 1 kA/cm^2 for both the measurement and TCAD simulation.

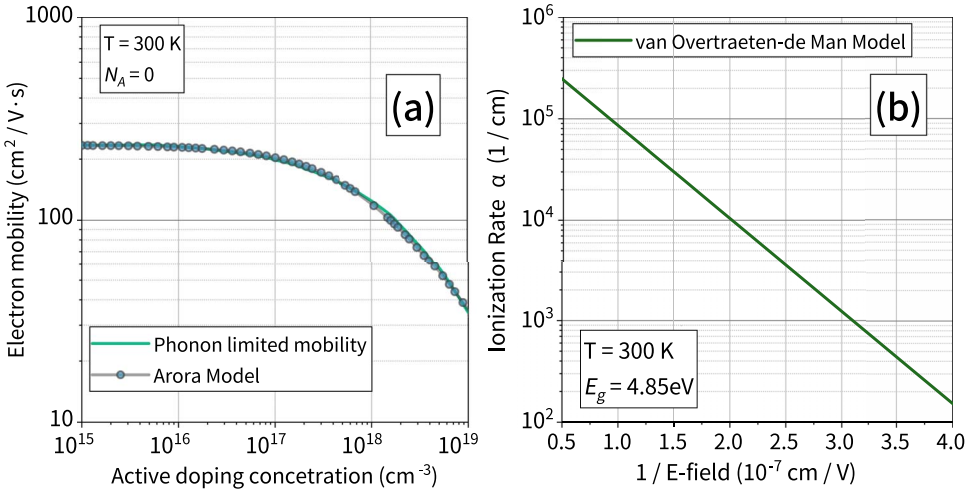

Figure 2. (a) Electron mobility as a function of the donor doping concentration at 300 K. The green line is obtained from the model.[38] Circles represent the results of the optimized Arora model used in this work. (b) The impact ionization coefficient for electrons, α, as a function of the inverse electric field (E-field^{-1}).

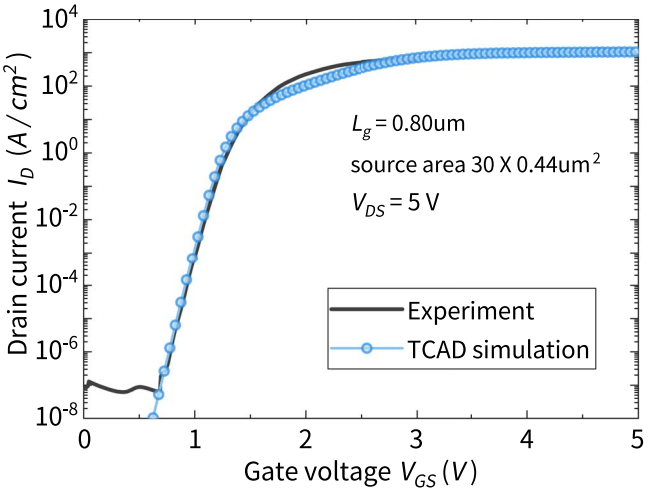

Figure 3. I_D-V_{GS} characteristics of the vertical $\beta - Ga_2O_3$ MOSFET in the semi-log scale. The fin width is 0.44 μm and the fin height is 0.8 μm. The drain voltage is 5 V. The line shows the experimental results[29] and the dot symbols are obtained by the TCAD simulation. Both the subthreshold slope and the threshold voltage are well matched.

Fig. 4 shows I_D-V_{DS} characteristics of the vertical $\beta - Ga_2O_3$ MOSFET. Various gate voltages (V_{GS}) from 0 V to 3.0 V are considered. The maximum drain current is 750 A/cm^2 at V_{GS} = 3 V and V_{DS} = 5 V. The channel differential on-resistance (R_{on}) near V_{DS} = 0 V is 7 $m\Omega \cdot cm^2$ for both the TCAD simulation and the experimental results.

The breakdown voltage is also evaluated. Although the bipolar simulation with the carrier generation due to the impact ionization is required for the rigorous evaluation of the breakdown voltage, the bipolar simulation of the Ga_2O_3 devices is found to be difficult from our numerical experience. In order to overcome such difficulty, an approximate estimation method for the impact ionization current is tried in this work.[47] The unipolar simulation only with electrons is performed without the impact ionization. Based upon the converged solution, the carrier generation rate due to the impact ionization is calculated as the post-process. By integrating the approximate generation rate over the entire structure, the avalanche current is evaluated.

Fig. 5 shows the impact ionization coefficient and the impact ionization rate. Since the impact ionization coefficient is sensitively dependent on the electric field as shown in (4), it exhibits the maximum value near the top surface of the drift region. However, the current density is strongly localized near the symmetric line. Therefore, the actual generation rate shown in Fig. 5b is also highly localized near the drain end of the fin. Fig. 6 shows the current due to the impact ionization, which is calculated by following the above-mentioned procedure. The structure with L_g = 0.8 μm and W_{ch} = 0.44 μm is simulated. Since the avalanche current exceeds the drain current without the impact ionization at about 400 V, the breakdown voltage is found to be 400 V. The estimated breakdown voltage, 400 V, is similar to the measured value.[29]

Up to now, it has been demonstrated that our simulation results are in close agreement with the available experimental results. Impact of the fin shape on the electrical characteristics is investigated in the subsequent sections.

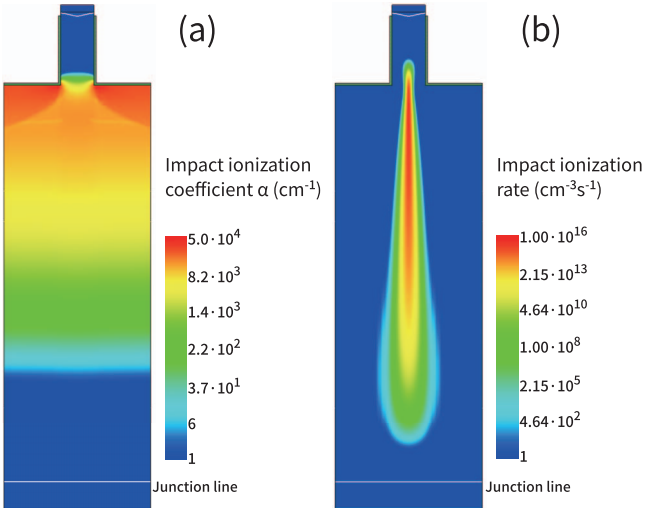

Figure 5. (a) Impact ionization coefficient α and (b) the impact ionization rate. The bias condition is V_{GS} = 0 V and V_{DS} = 400 V.

Optimization of fin shape.—As shown in the previous section, the $\beta - Ga_2O_3$ vertical MOSFET shows the enhanced operation mode and the high I_{on}. These attractive features are mainly due to the fin structure acting like a double-gated channel. While the extended drift region reduces the effective electric field within the channel, the fin structure determines the switch characteristics. In order to investigate the influence of the fin shape, the channel width (W_{ch}) and the fin height (L_g) of the fin structure are varied. The length of the underlap

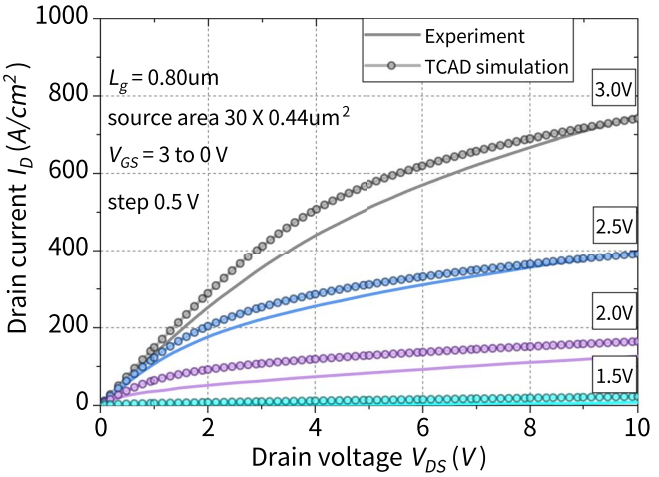

Figure 4. I_D-V_{DS} characteristics of the vertical $\beta - Ga_2O_3$ MOSFET. The simulated device is the same as that in Fig. 1. The lines show the experimental results[29] and the dot symbols are obtained from the TCAD simulations.

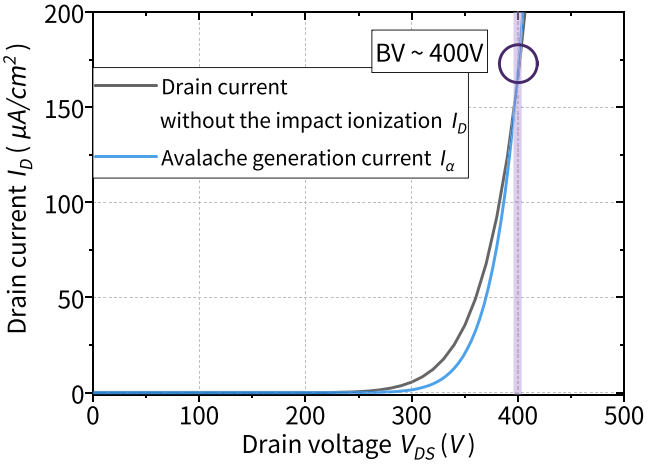

Figure 6. Typical example of the breakdown simulation. The drain current without the impact ionization (I_D) and the avalanche generation current (I_α) are shown. The gate voltage is 0 V.

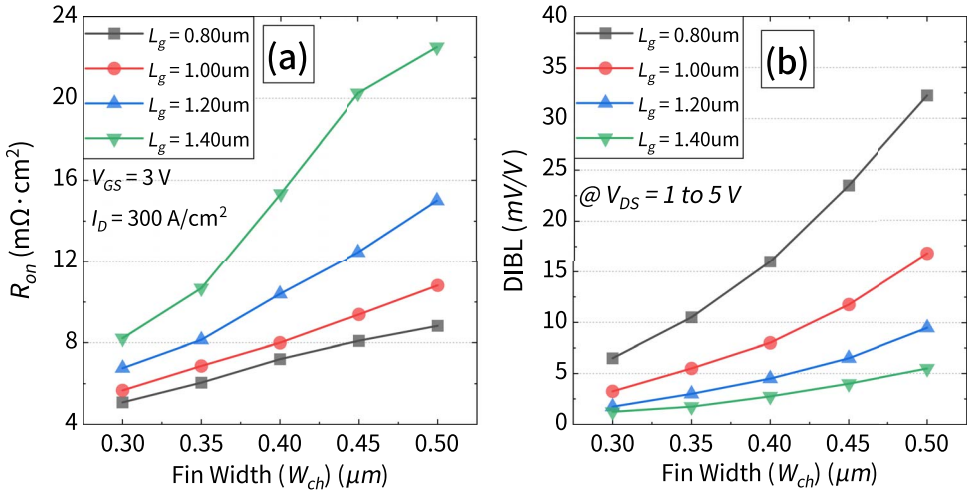

Figure 7. Comparison of the electrical characteristics. Various values of the fin height (L_g) and the fin width (W_{ch}) are tested. (a) The channel differential on-resistance R_{on} when $I_D = 300\ A/cm^2$ and (b) the DIBL characteristic. It is noted that the current and the on-resistance are normalized according to the source area.

region (0.1 μm) and the n^{++} doped source contact are not changed. In order to make a fair comparison of the devices with different sizes, the current and the on-resistance are normalized according to the source area.

Fig. 7 shows the device characteristics of various structures with different W_{ch} and L_g values. The on-resistance (R_{on}) is extracted at $I_D = 300\ A/cm^2$ and the drain-induced barrier lowering (DIBL) is evaluated between $V_{DS} = 1$ V and 5 V. Fig. 7a shows that the thinner W_{ch} improves the R_{on} characteristic. Conversely, an increased L_g leads an increase in the effective length of the channel, thereby increasing R_{on}. On the other hand, the DIBL is improved with a longer L_g. After the extensive simulation for various fin structures, it is found that a fin with $L_g = 1.0\ \mu m$ and $W_{ch} = 0.3\ \mu m$ is the optimal structure. While maintaining the low R_{on} per unit area, a very low DIBL (< 5 mV/V) can be achieved.

The $I_D - V_{GS}$ and $I_D - V_{DS}$ curves of the optimized fin structure are shown in Fig. 8. The I_D-V_{GS} curve in Fig. 8a shows that V_{th} increases from 0.92 V to 1.44 V. The SS characteristic has also been improved to 67 mV/dec. Moreover, the maximum channel current is improved from 1.1 kA/cm^2 to 1.5 kA/cm^2. A reduced fin width improves the on current characteristics. In the case of the $I_D - V_{DS}$ characteristic in Fig. 8b, the maximum drain current is also increased. The differential R_{on} at $V_{DS} = 0$ V decreases from 6.55 $m\Omega \cdot cm^2$ to 4.78 $m\Omega \cdot cm^2$.

Effect of tapered fin structure.—In the previous section, we have considered the perfectly rectangular shaped fins. In the fabrication process, many steps like the photolithography, the deposition, and the etching are required. Therefore, the fabricated fin is more likely to be tapered. It is important to understand the device characteristics depending on the shape of the tapered fin. The tapered fin structures are obtained by modifying the optimized fin in Optimization of fin shape section.

Fig. 9 shows the structure of the tapered fin used in the TCAD simulation. The average fin width is kept as 0.3 μm. The shape of the fin is varied by changing the internal angle between the drift channel region and the fin, as shown in Fig. 9a. When the internal angle is greater than 90°, the fin structure has an inverted trapezoidal shape which has a narrower interface with the drift region. Conversely, when the internal angle is less than 90°, the fin structure is trapezoidal.

Fig. 10 compares the device characteristics of various tapered fins. When the fin has the inverted trapezoidal shape (>90°), the effective width at the interface between the fin and the drift channel is reduced and R_{on} is increased. Conversely, when the fin is acute-angled (< 90°), which corresponds to a trapezoidal shape, the R_{on} characteristics are improved because the effective channel width increases at the contact surface. Also, as the channel width near the source is narrowed, the DIBL characteristics are also improved. If the fin has an inverted trapezoidal shape, the effective W_{ch} at the interface with the drift region is

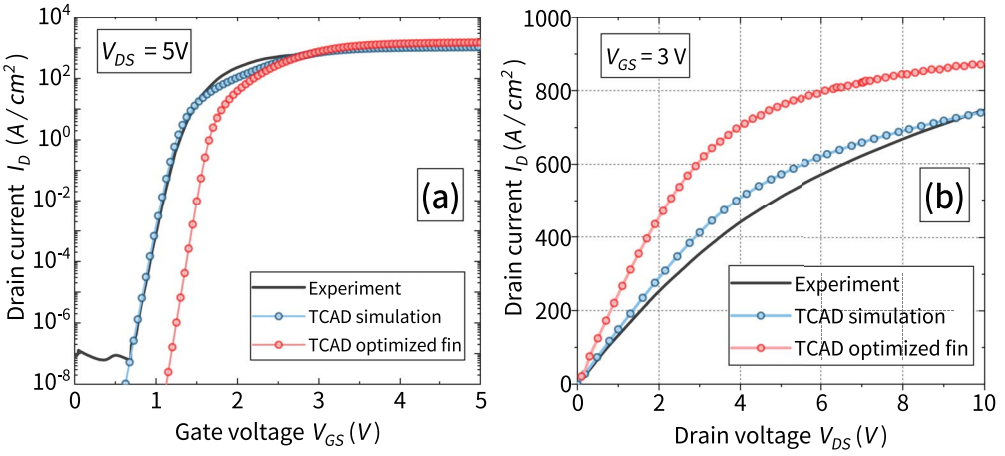

Figure 8. (a) I_D-V_{GS} and (b) I_D-V_{DS} curves of the optimized fin structure. The red circles represent the enhanced performance of the optimized fin shape.

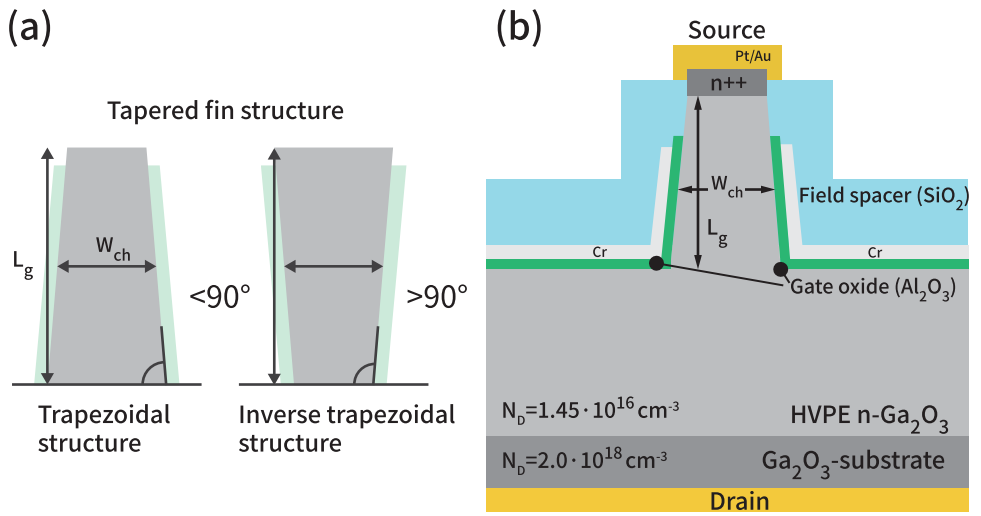

Figure 9. (a) Tapered fin structure. The internal angle of the tapered structure determines the fin shape. The average fin width at $L_g/2$ is fixed as W_{ch}. If the angle is less than 90°, it will have a trapezoidal fin, and if it is greater than 90°, an inverted trapezoidal fin is formed. (b) Simulated structure of the vertical FET with a trapezoidal fin (< 90° case).

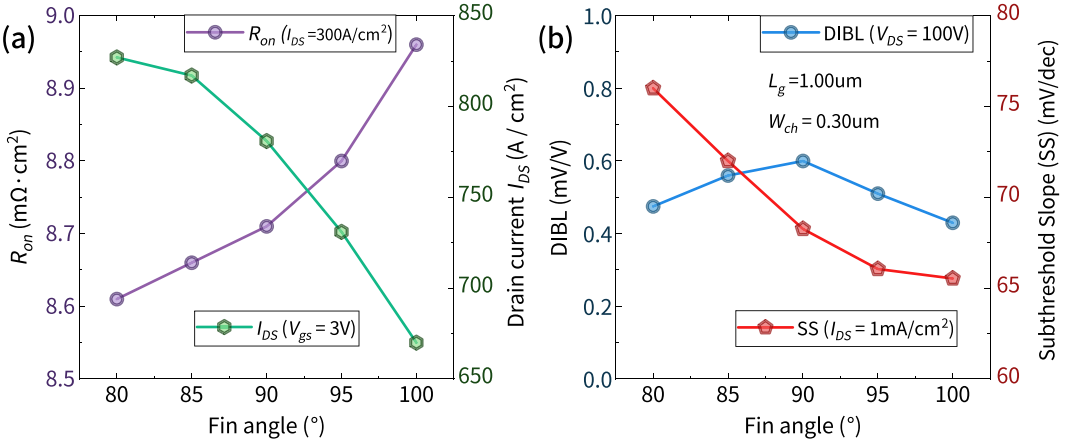

Figure 10. Device performance factors as functions of the internal fin angle. (a) R_{on} and saturated drain current I_D at $V_{GS} = 3$ V and $V_{DS} = 20$ V. (b) The DIBL and SS.

becomes narrower and it improves the SS characteristics. It can be observed that the gate controllability and the R_{on} characteristics have a trade-off relationship in the overall tapered fin structure.

Since the tapered fin structure changes the operating characteristics of the fin type vertical MOSFET significantly, a variation-tolerant design of the fin shape is desirable. It is expected that the TCAD simulation can contribute greatly in this aspect.

Conclusions

In summary, the simulation of the $\beta - Ga_2O_3$ vertical MOSFET with the fin shaped source has been presented. It has been shown that the fin shape (fin width, fin height, and tapered fin) changes the device characteristics considerably. It is expected that a vertical MOSFET with better performance can be designed with help of the TCAD simulation.

Acknowledgments

This research was supported by the Basic Science Research Program through the National Research Foundation of Korea (NRF) funded by the Ministry of Education (NRF-2018R1D1A1B07048277).

ORCID

Junsung Park https://orcid.org/0000-0001-7375-7520
Sung-Min Hong https://orcid.org/0000-0002-1840-085X

References

1. S. Stepanov, V. Nikolaev, V. Bougrov, and A. Romanov, "Gallium Oxide: Properties and Applications—A Review," *Reviews on Advanced Materials Science*, **44**, 63 (2016).
2. M. Higashiwaki, A. Kuramata, H. Murakami, and Y. Kumagai, "State-of-the-art technologies of gallium oxide power devices," *Journal of Physics D: Applied Physics*, **50**, 333002 (2017).
3. S. Pearton, J. Yang, P. H. Cary IV, F. Ren, J. Kim, M. J. Tadjer, and M. A. Mastro, "A review of Ga_2O_3 materials, processing, and devices," *Applied Physics Reviews*, **5**, 011301 (2018).
4. S. J. Pearton, F. Ren, M. Tadjer, and J. Kim, "Perspective: Ga_2O_3 for ultra-high power rectifiers and MOSFETS," *Journal of Applied Physics*, **124**, 220901 (2018).
5. M. Higashiwaki, K. Sasaki, A. Kuramata, T. Masui, and S. Yamakoshi, "Gallium oxide (Ga_2O_3) metal-semiconductor field-effect transistors on single-crystal $\beta - Ga_2O_3$(100) substrates," *Applied Physics Letters*, **100**, 013504 (2012).
6. Z. Guo, A. Verma, X. Wu, F. Sun, A. Hickman, T. Masui, A. Kuramata, M. Higashiwaki, D. Jena, and T. Luo, "Anisotropic thermal conductivity in single crystal β-gallium oxide," *Applied Physics Letters*, **106**, 111909 (2015).
7. E. G. Víllora, K. Shimamura, Y. Yoshikawa, K. Aoki, and N. Ichinose, "Large-size $\beta - ga_2o_3$ single crystals and wafers," *Journal of Crystal Growth*, **270**, 420 (2004).
8. Z. Galazka, K. Irmscher, R. Uecker, R. Bertram, M. Pietsch, A. Kwasniewski, M. Naumann, T. Schulz, R. Schewski, D. Klimm, and M. Bickermann, "On the bulk

$\beta - ga_2o_3$ single crystals grown by the czochralski method," *Journal of Crystal Growth*, **404**, 184 (2014).

9. K. Hoshikawa, E. Ohba, T. Kobayashi, J. Yanagisawa, C. Miyagawa, and Y. Nakamura, "Growth of $\beta - ga_2o_3$ single crystals using vertical bridgman method in ambient air," *Journal of Crystal Growth*, **447**, 36 (2016).
10. A. Kuramata, K. Koshi, S. Watanabe, Y. Yamaoka, T. Masui, and S. Yamakoshi, "High-quality $\beta - ga_2o_3$ single crystals grown by edge-defined film-fed growth," *Japanese Journal of Applied Physics*, **55**, 1202A2 (2016).
11. K. D. Chabak, N. Moser, A. J. Green, D. E. Walker, S. E. Tetlak, E. Heller, A. Crespo, R. Fitch, J. P. McCandless, K. Leedy, M. Baldini, G. Wagner, Z. Galazka, X. Li, and G. Jessen, "Enhancement-mode Ga_2O_3 wrap-gate fin field-effect transistors on native (100) $\beta - Ga_2O_3$ substrate with high breakdown voltage," *Applied Physics Letters*, **109**, 213501 (2016).
12. K. Chabak, A. Green, N. Moser, S. Tetlak, J. McCandless, K. Leedy, R. Fitch, A. Crespo, and G. Jessen, "Gate-recessed, laterally-scaled $\beta - Ga_2O_3$ MOSFETs with high-voltage enhancement-mode operation," 2017 75th Annual Device Research Conference (DRC), 1–2 (2017).
13. W. Li, Z. Hu, K. Nomoto, R. Jinno, Z. Zhang, T. Q. Tu, K. Sasaki, A. Kuramata, D. Jena, and H. G. Xing, "2.44 kV Ga_2O_3 vertical trench Schottky barrier diodes with very low reverse leakage current," in 2018 IEEE International Electron Devices Meeting (IEDM) (2018) pp. 8.5.1–8.5.4.
14. H. Xue, Q. He, G. Jian, S. Long, T. Pang, and M. Liu, "An Overview of the Ultrawide Bandgap Ga_2O_3 Semiconductor-Based Schottky Barrier Diode for Power Electronics Application," *Nanoscale Research Letters*, **13**, 290 (2018).
15. Y.-W. Huan, S.-M. Sun, C.-J. Gu, W.-J. Liu, S.-J. Ding, H.-Y. Yu, C.-T. Xia, and D. W. Zhang, "Recent advances in Ga_2O_3–metal contacts," *Nanoscale Research Letters*, **13**, 246 (2018).
16. J. Yang, F. Ren, S. J. Pearton, and A. Kuramata, "Vertical Geometry, 2-A Forward Current Ga_2O_3 Schottky Rectifiers on Bulk Ga_2O_3 Substrates," *IEEE Transactions on Electron Devices*, **65**, 2790 (2018).
17. J. Yang, F. Ren, M. Tadjer, S. J. Pearton, and A. Kuramata, "300 V Reverse Breakdown Voltage Ga_2O_3 Schottky Rectifiers," *ECS Journal of Solid State Science and Technology*, **7**, Q92 (2018).
18. Y. Zhang, C. Joishi, Z. Xia, M. Brenner, S. Lodha, and S. Rajan, "Demonstration of $\beta - (Al_xGa_{1-x})_2O_3/Ga_2O_3$ double heterostructure field effect transistors," *Applied Physics Letters*, **112**, 233503 (2018).
19. M. H. Wong, K. Sasaki, A. Kuramata, S. Yamakoshi, and M. Higashiwaki, "Field-Plated Ga_2O_3 MOSFETs With a Breakdown Voltage of Over 750 V," *IEEE Electron Device Letters*, **37**, 212 (2016).
20. K. Zeng, A. Vaidya, and U. Singisetti, "710 V Breakdown Voltage in Field Plated Ga203 MOSFET," in *2018 76th Device Research Conference (DRC)* pp. 1–2 (2018).
21. K. Zeng, A. Vaidya, and U. Singisetti, "1.85 kV Breakdown Voltage in Lateral Field-Plated Ga_2O_3 MOSFETs," *IEEE Electron Device Letters*, **39**, 1385 (2018).
22. M. Singh, M. A. Casbon, M. J. Uren, J. W. Pomeroy, S. Dalcanale, S. Karboyan, P. J. Tasker, M. H. Wong, K. Sasaki, A. Kuramata, S. Yamakoshi, M. Higashiwaki, and M. Kuball, "Pulsed Large Signal RF Performance of Field-Plated Ga_2O_3 MOSFETs," *IEEE Electron Device Letters*, **39**, 1572 (2018).
23. Y. Lv, X. Zhou, S. Long, X. Song, Y. Wang, S. Liang, Z. He, T. Han, X. Tan, Z. Feng, H. Dong, X. Zhou, Y. Yu, S. Cai, and M. Liu, "Source-Field-Plated β-Ga2O3 MOSFET With Record Power Figure of Merit of 50.4 MW/cm^2," *IEEE Electron Device Letters*, **40**, 83 (2019).
24. K. Zeng, K. Sasaki, A. Kuramata, T. Masui, and U. Singisetti, "Depletion and enhancement mode $\beta - Ga_2O_3$ MOSFETs with ALD SiO2 gate and near 400 V breakdown voltage," 2016 74th Annual Device Research Conference (DRC), 1–2 (2016).
25. K. D. Chabak, J. P. McCandless, N. A. Moser, A. J. Green, K. Mahalingam, A. Crespo, N. Hendricks, B. M. Howe, S. E. Tetlak, K. Leedy, R. C. Fitch, D. Wakimoto, K. Sasaki, A. Kuramata, and G. H. Jessen, "Recessed-Gate Enhancement-Mode $\beta - Ga_2O_3$ MOSFETs," *IEEE Electron Device Letters*, **39**, 67 (2018).
26. M. H. Wong, K. Goto, A. Kuramata, S. Yamakoshi, H. Murakami, Y. Kumagai, and M. Higashiwaki, "First demonstration of vertical Ga_2O_3 MOSFET: Planar structure with a current aperture," in 2017 75th Annual Device Research Conference (DRC), pp. 1–2 (2017).
27. M. H. Wong, Y. Nakata, A. Kuramata, S. Yamakoshi, and M. Higashiwaki, "Enhancement-mode Ga_2O_3 MOSFETs with Si-ion-implanted source and drain," *Applied Physics Express*, **10**, 041101 (2017).
28. K. Sasaki, Q. T. Thieu, D. Wakimoto, Y. Koishikawa, A. Kuramata, and S. Yamakoshi, "Depletion-mode vertical Ga_2O_3 trench MOSFETs fabricated using Ga_2O_3 homoepitaxial films grown by halide vapor phase epitaxy," *Applied Physics Express*, **10**, 124201 (2017).
29. Z. Hu, K. Nomoto, W. Li, N. Tanen, K. Sasaki, A. Kuramata, T. Nakamura, D. Jena, and H. G. Xing, "Enhancement-Mode Ga_2O_3 Vertical Transistors With Breakdown Voltage > 1 kV," *IEEE Electron Device Letters*, **39**, 869 (2018).
30. Z. Hu, K. Nomoto, W. Li, Z. Zhang, N. Tanen, Q. T. Thieu, K. Sasaki, A. Kuramata, T. Nakamura, D. Jena, and H. G. Xing, "Breakdown mechanism in 1 kA/cm^2 and 960 V E-mode $\beta - Ga_2O_3$ vertical transistors," *Applied Physics Letters*, **113**, 122103 (2018).
31. M. H. Wong, K. Goto, H. Murakami, Y. Kumagai, and M. Higashiwaki, "Current Aperture Vertical $\beta - Ga_2O_3$ MOSFETs Fabricated by N- and Si-Ion Implantation Doping," *IEEE Electron Device Letters*, 1–1 (2018).
32. J. F. Mcglone, Z. Xia, Y. Zhang, C. Joishi, S. Lodha, S. Rajan, S. A. Ringel, and A. R. Arehart, "Trapping Effects in Si δ-Dopedβ-Ga_2O_3 MESFETs on an Fe-Doped β-Ga_2O_3 Substrate," *IEEE Electron Device Letters*, **39**, 1042 (2018).
33. I. Lee, A. Kumar, K. Zeng, U. Singisetti, and X. Yao, "Mixed-mode circuit simulation to characterize Ga_2O_3 MOSFETs in different device structures," in 2017 IEEE 5th Workshop on Wide Bandgap Power Devices and Applications (WiPDA) (2017) pp. 185–189 .
34. H. Wang, L.-L. Jiang, X.-P. Lin, S.-Q. Lei, and H.-Y. Yu, "A simulation study of field plate termination in Ga_2O_3 Schottky barrier diodes," *Chinese Physics B*, **27**, 127302 (2018).
35. J.-H. Choi, C.-H. Cho, and H.-Y. Cha, "Design consideration of high voltage Ga_2O_3 vertical Schottky barrier diode with field plate," *Results in Physics*, **9**, 1170 (2018).
36. H. Y. Wong, N. Braga, R. V. Mickevicius, and F. Ding, "Normally-OFF dual-gate Ga_2O_3 planar MOSFET and FinFET with high I_{ON} and BV," in 2018 IEEE 30th International Symposium on Power Semiconductor Devices and ICs (ISPSD) pp. 379–382 (2018).
37. A. Parisini and R. Fornari, "Analysis of the scattering mechanisms controlling electron mobility in$\beta - Ga_2O_3$ crystals," *Semiconductor Science and Technology*, **31**, 035023 (2016).
38. N. Ma, N. Tanen, A. Verma, Z. Guo, T. Luo, H. G. Xing, and D. Jena, "Intrinsic electron mobility limits in $\beta - Ga_2O_3$," *Applied Physics Letters*, **109**, 212101 (2016).
39. K. Ghosh and U. Singisetti, "Ab initio calculation of electron–phonon coupling in monoclinic $\beta - Ga_2O_3$ crystal," *Applied Physics Letters*, **109**, 072102 (2016).
40. K. Ghosh and U. Singisetti, "Electron mobility in monoclinic $\beta - Ga_2O_3$—Effect of plasmon-phonon coupling, anisotropy, and confinement," *Journal of Materials Research*, **32**, 4142 (2017).
41. Y. Kang, K. Krishnaswamy, H. Peelaers, and C. G. V. de Walle, "Fundamental limits on the electron mobility of $\beta - Ga_2O_3$," *Journal of Physics: Condensed Matter*, **29**, 234001 (2017).
42. N. D. Arora, J. R. Hauser, and D. J. Roulston, "Electron and hole mobilities in silicon as a function of concentration and temperature," *IEEE Transactions on Electron Devices*, **29**, 292 (1982).
43. D. M. Caughey and R. E. Thomas, "Carrier mobilities in silicon empirically related to doping and field," *Proceedings of the IEEE*, **55**, 2192 (1967).
44. K. Ghosh and U. Singisetti, "Impact ionization in $\beta - Ga_2O_3$," *Journal of Applied Physics*, **124**, 085707 (2018).
45. K. A. Mengle and E. Kioupakis, "Vibrational and electron-phonon coupling properties of $\beta - Ga_2O_3$ from first-principles calculations: Impact on the mobility and breakdown field," *AIP Advances*, **9**, 015313 (2019).
46. Synopsys, "Sentaurus User's Manual, Version. O-2018.06," Mountain View, CA **O-2018.06** (2018).
47. S.-M. Hong, A.-T. Pham, and C. Jungemann, *Deterministic solvers for the Boltzmann transport equation* Springer-Verlag (2011).